

# Extraction of high-silica granites from an upper crustal magma reservoir: Insights from the Narusongduo magmatic system, Gangdese arc

JIN-SHENG ZHOU<sup>1,2</sup>, ZHU-SEN YANG<sup>3,\*</sup>, QIANG WANG<sup>1,4,5,\*</sup>, YUAN-CHUAN ZHENG<sup>6</sup>, ZENG-QIAN HOU<sup>2</sup>, AND DEREK A. WYMAN<sup>7</sup>

<sup>1</sup>State Key Laboratory of Isotope Geochemistry, Guangzhou Institute of Geochemistry, Chinese Academy of Sciences, Guangzhou 510640, China

<sup>2</sup>Institute of Geology, Chinese Academy of Geological Sciences, Beijing 100037, China

<sup>3</sup>MLR Key Laboratory of Metallogeny and Mineral Assessment, Institute of Mineral Resources, Chinese Academy of Geological Sciences, Beijing 100037, China

<sup>4</sup>CAS Center for Excellence in Tibetan Plateau Earth Sciences, Beijing 100101, China

<sup>5</sup>College of Earth and Planetary Sciences, University of Chinese Academy of Sciences, Beijing 100049, China

<sup>6</sup>School of Earth Science and Resources, China University of Geosciences, Beijing 100083, China

<sup>7</sup>School of Geosciences, The University of Sydney, New South Wales 2006, Australia

## ABSTRACT

The genesis of high-silica igneous rocks is important for understanding the behavior of shallow magmatic systems. However, although many such studies have focused on the eruption of crystal-poor high-SiO<sub>2</sub> rhyolites, the origin of high-silica granites (HSGs) has received comparatively little attention. Here, we present a detailed study of HSGs from the Narusongduo volcanic complex, Gangdese arc. Combining zircon U-Pb geochronology with stratigraphic investigations, we show that the Narusongduo magmatic system was constructed over a period of  $\geq 3.7$  Myr with or without lulls. On the basis of zircon textures and ages, diverse zircon populations, including antecrysts and autocrysts, are recognized within the HSGs and volcanic rocks. All of the igneous rocks within the Narusongduo volcanic complex have highly radiogenic Sr–Nd isotopic compositions. Our results indicate the presence of an andesitic magma reservoir in the upper crust at a paleodepth of  $\sim 8$  km. Ubiquitous zircon antecrysts in the HSGs, combined with compositional similarities between the HSGs and evolved melts of the andesitic magma reservoir, indicate that the Narusongduo HSGs represent melts extracted from the shallow magma reservoir. In addition, our results suggest that magma recharge promoted the escape of high-silica melts to form the Narusongduo HSGs. This work presents an excellent case that kilometer-scale high-silica granites are the differentiated products from an upper crustal magma reservoir. It would make a contribution to contemporary debates concerning the efficiency of crystal–melt separation in upper crustal magmatic systems.

**Keywords:** High-silica granite, magma reservoir, crystal–melt separation, upper crust, rhyolite

## INTRODUCTION

High-silica granites (HSGs) and rhyolites, although comprising a small proportion of the upper continental crust, are important for understanding the behavior of shallow magmatic systems. Their study can test the efficiency of crystal–melt separation within upper-crustal magma reservoirs (Bachmann and Huber 2019). In crustal magmatic systems, heat is one of the main controlling factors and determines rheological properties and dynamic behavior of magmas (e.g., Caricchi and Blundy 2015; Blundy and Annen 2016). Thus melt segregation in hot, deep crust is efficient, where chemical differentiation is achieved through crystal fractionation of primitive magmas and/or partial melting of crustal rocks (Hildreth and Moorbath 1988; Annen et al. 2006).

In contrast, large-scale extraction of residual melts from upper-crustal magma bodies is currently debated. The obvious thermal problems might be reconciled by the existence of a long-lived (several million years) transcrustal magmatic system

that would facilitate the formation of a magma reservoir with prolonged survivability in the upper crust (e.g., de Silva and Gregg 2014; Karakas et al. 2017). In such a case of a thermally mature system, the time needed for phase separation to occur might be enough (Bachmann and Huber 2019). Compaction is widely invoked as an efficient mechanism for driving separation of melt in silicic magma reservoirs (e.g., Miller et al. 1988; Bachmann and Bergantz 2004). However, there is little microstructural evidence in support of widespread compaction in the solidification of silicic magma chambers (Holness 2018), although this argument against compaction is not widely accepted (e.g., Sparks et al. 2019).

Field examples can help in understanding the dynamic behavior of shallow magmatic systems. Studies of large-scale evolved melts that were segregated from upper-crustal magma bodies have focused on crystal-poor high-SiO<sub>2</sub> rhyolites (e.g., Hildreth 1979; Lipman 1988; Bachmann and Bergantz 2004; Deering et al. 2011). In contrast, convincing examples of their intrusive counterparts, representing the separation of highly evolved melts at shallow crustal levels to form pluton-scale

\* E-mail: yangzhusenyx@163.com and wqiang@gig.ac.cn

granites, are scarce. HSGs are commonly exposed in the roof or core of zoned intrusive suites (e.g., Miller and Miller 2002; Putirka et al. 2014) and have traditionally been interpreted to represent upward percolation of evolved melts (e.g., Bateman and Chappell 1979; Hildreth 1981; Barnes 1983). However, petrographic variability in zoned intrusive suites can also be ascribed to incremental intrusion, and HSGs may represent discrete magmatic pulses from their lower-crustal source rather than the products of in situ differentiation (e.g., Clemens and Stevens 2012; Coleman et al. 2012). Thus, identification of pluton-scale HSGs that represent melts extracted from upper-crustal magma reservoirs is important for testing the efficiency of crystal–melt separation in shallow magmatic systems.

Here, we present an excellent case that kilometer-scale HSG bodies are the differentiated products derived from a shallow intermediate magma reservoir, which is located within the Narusongduo volcanic complex, Gangdese arc, Tibet. In this study, we combine field, geochronologic, mineral, and geochemical data to provide a quantified petrologic reconstruction of the Narusongduo magmatic system, with particular focus on the genesis of HSGs.

## GEOLOGICAL BACKGROUND

The Gangdese arc, in the southern Tibetan Plateau, is a remnant of a Triassic–Tertiary continental arc that was sandwiched between the Indian and Asian plates during continental collision. It contains voluminous volcanic rocks that overlie predominantly felsic plutons and extends along strike for more than 1500 km (e.g., Hou et al. 2015; Zhu et al. 2017). Triassic to early Tertiary magmatism in the Gangdese arc originated through northward subduction of the Neo-Tethyan Ocean lithosphere along the southern margin of the Lhasa Terrane (e.g., Chung et al. 2005; Hou et al. 2015). Radiometric age data from intrusive and volcanic rocks show that arc magmatism began during the Late Triassic and lasted until the Paleocene (Chung et al. 2005; Ji et al. 2009; Zhu et al. 2017). Several periods of magmatic activity are recorded that reflect the episodic construction of the Gangdese batholith (e.g., Hou et al. 2015; Zhu et al. 2017), although the most intense phase of magmatism occurred during the early Tertiary (Mo et al. 2008; Zhu et al. 2017). Most of the volcanic rocks are Tertiary in age (Fig. 1a), with compositions that vary mainly from andesite to rhyolite with calc-alkaline to high-K calc-alkaline signatures (e.g., Wang et al. 2015; Zhu et al. 2015). The Gangdese batholith contains gabbro, diorite, granodiorite, and monzogranite and/or syenogranite, (e.g., Ji et al. 2009), as well as peraluminous leucogranites (e.g., Ma et al. 2018). With the aim of determining the petrogenesis of the HSGs, we conducted a case study on rocks from the Narusongduo volcanic complex (Fig. 1b), located within the central Gangdese arc (Fig. 1a).

## SAMPLING AND METHODS

### Sampling

We performed detailed field mapping and several stratigraphic investigations, establishing that the Narusongduo volcanic field, though eroded, covers ~245 km<sup>2</sup> and has a cumulative thickness of 948 m, with an estimated present-day volume of ~232 km<sup>3</sup>. The Narusongduo HSGs occur as isolated plutons with diameters less than 1.5 km (Fig. 1b). Most HSGs are porphyritic and dominated by phenocrysts of quartz, altered feldspar, and biotite, in a matrix of finer-grained quartz and feldspar.

Large volumes of intermediate volcanic rocks surround the HSGs (Fig. 1b), comprising dacitic to andesitic lavas, breccias, crystal tuffs, and tuffaceous sandstones and siltstones. The dacites are vitrophyric, with a mineral assemblage consisting of plagioclase, magnetite, and zircon with or without quartz, clinopyroxene, and amphibole. The andesites exhibit a hyalopilitic texture and contain plagioclase, clinopyroxene, and Fe-Ti oxides, with variable amounts of amphibole, quartz, and zircon. Plagioclase is the most abundant phenocryst in the andesites and shows complex zoning patterns and sieve textures (Supplemental<sup>1</sup> Figs. S1a and S1b). Clinopyroxene is the second most abundant type of phenocryst. Notably, the andesites also contain two types of glomerocrysts, comprising clinopyroxene plus plagioclase and amphibole plus quartz (Supplemental<sup>1</sup> Figs. S1c, S1d, and S1f). Fresh samples of HSG, dacite, and andesite were collected for whole-rock major-element, trace-element, and Sr-Nd isotope geochemistry, zircon U–Pb dating, and mineral chemistry.

### Analytical methods

Zircon U–Pb dating used a combination of secondary ionization mass spectrometry (SIMS) and laser ablation–inductively coupled plasma–mass spectrometry (LA–ICP–MS) techniques. SIMS analyses were performed using a CAMECA IMS 1280-HR at the State Key Laboratory of Isotope Geochemistry (SKLaBIG), Guangzhou Institute of Geochemistry, Chinese Academy of Sciences (GIG–CAS), Guangzhou, China. Analytical procedures followed those described by Li et al. (2009). The O<sub>2</sub> primary ion beam was accelerated at 13 kV with an intensity of ~10 nA, and the spot size was ~20 × 30 μm. Zircon U–Th–Pb isotopic ratios were determined relative to the Plešovice standard (Sláma et al. 2008). A reference standard (Qinghu; Li et al. 2013) was measured alongside the unknown samples, and two sets of measurements yielded concordia ages of 159.2 ± 1.5 and 159.4 ± 2.1 Ma, within the uncertainty of the recommended age (159.5 ± 0.2 Ma). LA–ICP–MS analyses were conducted using a Finnegan Neptune multi-collector ICP–MS instrument with a Newwave UP 213 LA system at the Institute of Mineral Resources, Chinese Academy of Geological Sciences, Beijing, China. Analyses used a beam diameter of 25 μm, a repetition rate of 10 Hz, and an energy of 2.5 J/cm<sup>2</sup>. Zircon GJ-1 was used as an internal standard during analysis. Further details are provided in the Supplemental Materials.

Whole-rock major- and trace-element analyses were performed at the Wuhan SampleSolution Analytical Technology Co. Ltd., Wuhan, China, and the Analytical Laboratory Beijing Research Institute of Uranium Geology, Beijing, China. Major-element compositions were determined using X-ray fluorescence spectrometry, whereas trace-element analyses were conducted via ICP–MS; in either case, with the exceptions of Li, Cr, Cu, Cs, and Tl, most elements have a precision of better than 5%.

Most whole-rock Sr and Nd isotopic compositions were determined at the SKLaBIG, GIG–CAS, following the analytical procedures of Li et al. (2006). All Sr and Nd isotopic ratios were normalized to values of <sup>86</sup>Sr/<sup>88</sup>Sr = 0.1194 and <sup>146</sup>Nd/<sup>144</sup>Nd = 0.7219, respectively. The measured composition of the Sr (NBS-987) and Nd (Shin Etsu Jndi-1) standards were 0.710261 ± 13 (2σ; n = 10) and 0.512115 ± 6 (2σ; n = 10), respectively. The USGS reference standard BHVO-2 was analyzed as an unknown and gave <sup>86</sup>Sr/<sup>88</sup>Sr = 0.703476 ± 0.000012 and <sup>146</sup>Nd/<sup>144</sup>Nd = 0.512900 ± 0.000004, consistent with the recommended values (<sup>87</sup>Sr/<sup>86</sup>Sr = 0.703481 ± 0.000020, <sup>143</sup>Nd/<sup>144</sup>Nd = 0.512983 ± 0.000010; Weis et al. 2005). A further four Sr–Nd analyses were performed at the State Key Laboratory for Mineral Deposit Research at Nanjing University, Nanjing, China. Detailed analytical procedures can be found in the Supplemental Materials<sup>1</sup>.

Compositional profiles across selected plagioclase grains were analyzed for major elements, including Mg contents using a Cameca SXFiveFE electron microprobe at the SKLaBIG, GIG–CAS. The Mg content was measured using a counting time of 120 s, yielding a detection limit of 34–36 ppm. Other mineral compositions were determined using a JEOL JXA-8800 Superprobe at the Institute of Mineral Resources, Chinese Academy of Geological Sciences, Beijing, China. Further details are provided in the Supplemental Materials. Cathodoluminescence (CL) images of zircon and quartz were obtained using a Zeiss SUPRA55SAPPHIR Field Emission Scanning Electron Microscope (FESEM) + Gatan MonoCL4 at the SKLaBIG, GIG–CAS, using 60 s capture time, with an image resolution of 2048 × 1536 pixels. Mineral trace-element compositions were analyzed using an ELEMENT XR (Thermo-Fisher Scientific) ICP–SF–MS instrument coupled with a 193 nm (ArF) Resonetics RESOLUTION M-50 LA system at the SKLaBIG, GIG–CAS. A spot size of 33 μm was employed at a pulse energy of ~4 J cm<sup>-2</sup> and a laser repetition rate of 5 Hz. The BCR-2G, GSD-1G, and BHVO-2G standards were measured to establish a calibration line for all elements. Analysis of USGS reference glass TB-1G as an unknown sample indicated that most trace elements

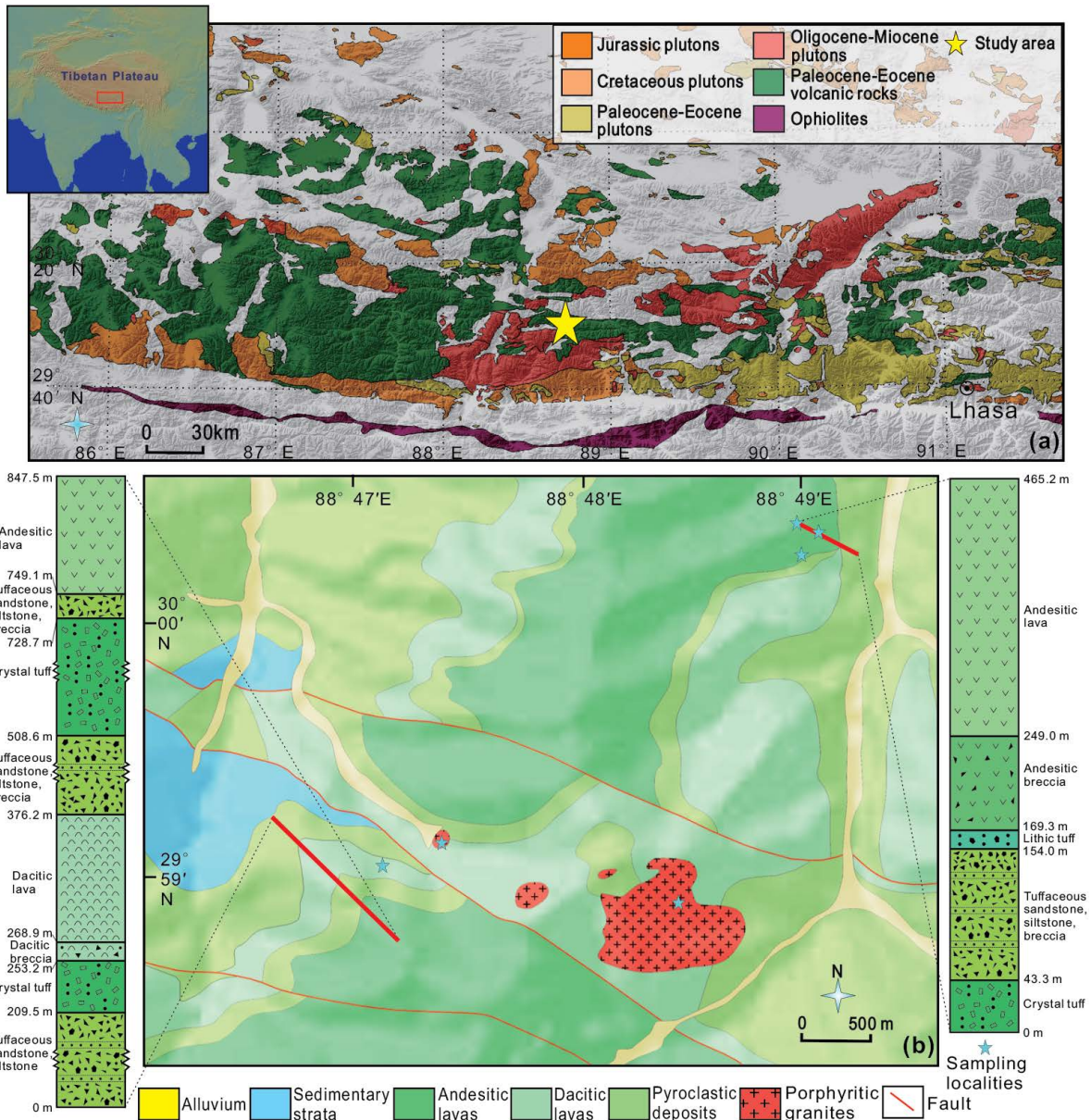


**FIGURE 1.** (a) Geological map showing plutonic and volcanic suites of the central Gangdese arc, Tibet. The inset map shows the location of the central Gangdese arc. The yellow star shows the location of the Narusongduo volcanic complex. (b) Geological map of a part of the Narusongduo volcanic complex, showing stratigraphic investigations and sampling localities. The blue stars represent sample localities. All porphyritic granites are high-silica granites. (Color online.)

are within 10% of the recommended values, with an analytical precision (2RSD, relative standard deviations) of better than 12%. Detailed analytical procedures and data reduction strategies are similar to those of Zhang et al. (2019). The  $\text{SiO}_2$  contents (from electron microprobe analyses) were utilized as the internal standard when normalizing trace-element concentrations.

## RESULTS

### Treatment of zircon U–Pb data

A total of 181 zircon crystals from six samples representing the three main igneous units within the Narusongduo volcanic complex were analyzed, including 127 SIMS analyses and 54

LA–ICP–MS analyses. All zircon U–Pb data are presented in Supplemental<sup>1</sup> Table S1. Previously published zircon U–Pb data for the Narusongduo HSGs (sample NRSDIII09-1-1) are shown for comparison (compiled from Ji et al. 2012; Fig. 2). Zircon crystals from the HSGs have sizes of ~50 to ~200  $\mu\text{m}$  along the length and diverse aspect ratios. CL imaging of the internal textures of representative zircon crystals in the HSGs allowed two main populations to be defined (Supplemental<sup>1</sup> Fig. S2), one with bright CL responses and another with dark CL responses. Some crystals also exhibit CL-bright interiors with CL-dark

overgrowths (Supplemental<sup>1</sup> Fig. S2). Zircon crystals from the andesites and dacites commonly show oscillatory zoning in CL, and discrete zircon populations are not clearly identifiable.

If all zircon crystals crystallized from a single magma pulse and the system conforms to closed-system behavior, then the quality of geochronological data can be evaluated by statistical measures, such as the mean square of weighted deviates (MSWD; Wendt and Carl 1991), which is near 1.0 when the goodness of fit is perfect. However, in a multi-cyclic magmatic system, various crystal populations might be expected (e.g., Miller et al. 2007), including xenocrysts, antecrysts, and autocrysts (the terminology recommended by Miller et al. 2007), as the case of this study (Supplemental<sup>1</sup> Fig. S2). Thus, we employed the Unmix Ages algorithm of Sambridge and Compston (1994), as implemented in Isoplot 4.15 (Ludwig 2003), to obtain age components of different zircon populations. The classical weighted average was used if calculated age components are essentially equal (within error of each other). The results are shown in Figure 2 with  $2\sigma$  errors.

Zircon grains from some HSGs fall into two main populations. Two samples yield younger populations of  $62.6 \pm 0.8$  and  $61.7 \pm 0.6$  Ma, with older populations of  $66.6 \pm 1.2$  and  $66.9 \pm 1.6$  Ma, respectively. One HSGs sample has a weighted mean  $^{206}\text{Pb}/^{238}\text{U}$  age of  $62.7 \pm 0.4$  Ma (MSWD = 0.49,  $n = 31$ ). Grains from the two andesite samples also contain older populations with ages of  $69.3 \pm 0.9$  and  $66.5 \pm 1.5$  Ma. However, three andesite samples yield near-identical younger ages of  $63.4 \pm 1.1$ ,  $63.2 \pm 0.6$ , and  $63.3 \pm 1.1$  Ma, respectively. One dacite sample yielded a weighted mean  $^{206}\text{Pb}/^{238}\text{U}$  age of  $65.4 \pm 0.4$  Ma (MSWD = 0.87,  $n = 32$ ).

### Whole-rock geochemistry

The whole-rock major- and trace-element compositions of the Narusongduo HSGs and volcanic rocks are presented in Supplemental<sup>1</sup> Table S2. The Narusongduo HSGs have high  $\text{SiO}_2$  contents (79.5–83.9 wt%  $\text{SiO}_2$ ) and low Zr/Hf ratios (22.5–37.0; Supplemental<sup>1</sup> Table S2). The anomalously high  $\text{SiO}_2$  contents of the HSGs suggest alteration, so we restrict our discussion

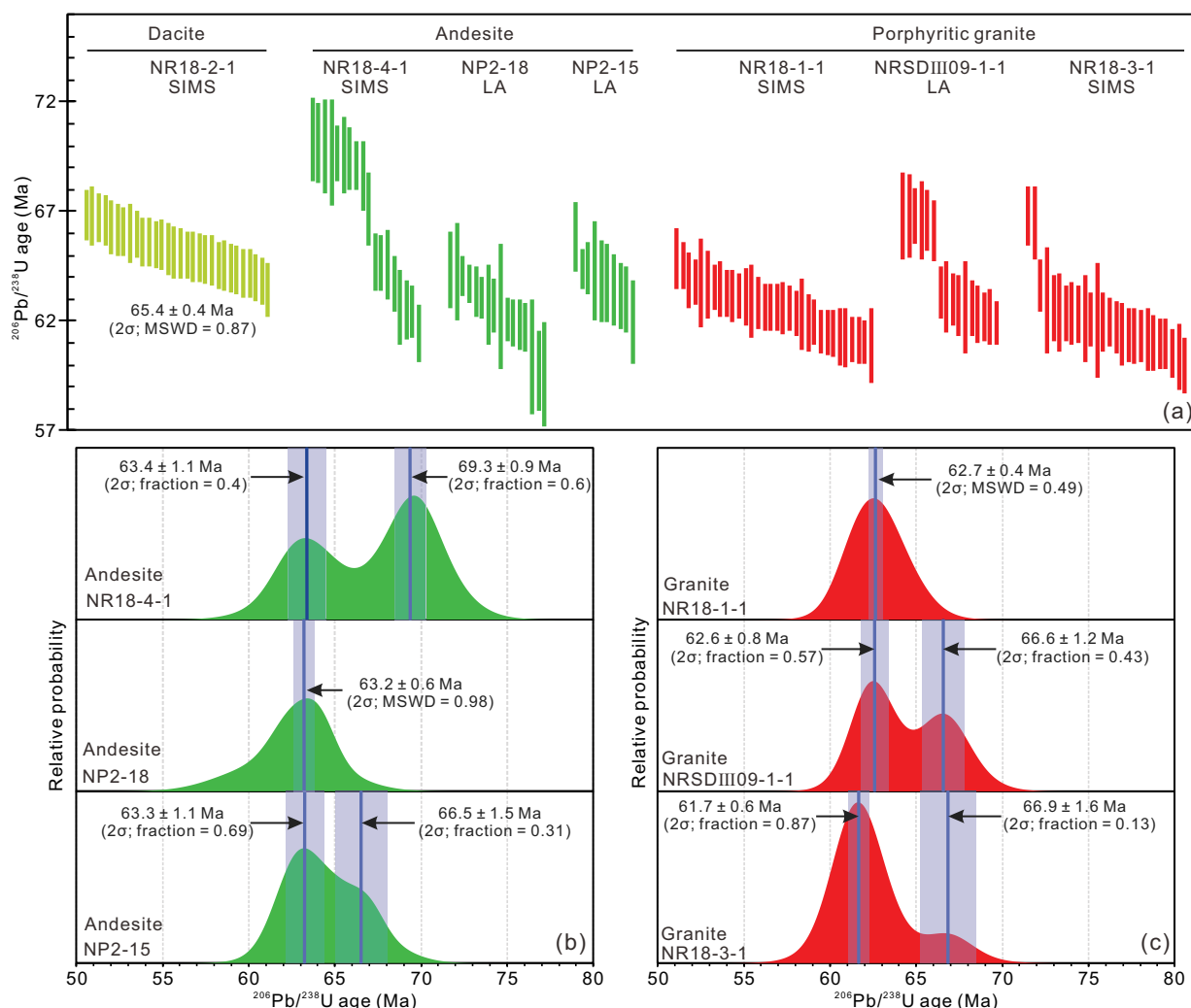


**FIGURE 2.** (a) Rank order plot of individual zircon SIMS and LA-ICP-MS  $^{206}\text{Pb}/^{238}\text{U}$  dates. The data from one dacite sample (NR18-2-1) are shown along with a corresponding weighted mean age. (b) and (c) Probability density function plots of zircon  $^{206}\text{Pb}/^{238}\text{U}$  dates with errors (blue regions) for samples andesite and HSGs. Age components of different zircon populations were calculated using the Unmix Ages algorithm of Sambridge and Compston (1994). The previously published zircon U–Pb data for HSGs (sample NRSDIII09-1-1) are compiled from Ji et al. (2012). (Color online.)



to concentrations or ratios of rare-earth elements (REEs) and high field strength elements (HFSEs), which are insensitive to alteration. On chondrite-normalized REE plots (Fig. 3), the HSGs are enriched in light REEs (LREEs) relative to heavy REEs (HREEs) and show pronounced negative Eu anomalies ( $\text{Eu}/\text{Eu}^* = 0.11\text{--}0.47$ ).  $\text{SiO}_2$  contents of the andesites vary from 55.1 to 56.5 wt%, with Zr/Hf values in the range 31.9 to 40.9. The dacitic units are characterized by a wide range of major-element compositions, with  $\text{SiO}_2$  contents varying from 64.3 to 73.8 wt% and Zr/Hf values ranging from 34.7 to 38.7. The andesitic and dacitic rocks have similar REE patterns for which Eu anomalies are weak or absent (Fig. 3).

Whole-rock Sr–Nd isotopic compositions are presented in Supplemental<sup>1</sup> Table S3. Owing to high Rb/Sr ratios ( $\text{Rb}/\text{Sr} = 4.1\text{--}20.5$ ; Supplemental<sup>1</sup> Table S3) and radiogenic ingrowth, the HSGs have elevated  $^{87}\text{Sr}/^{86}\text{Sr}$  ratios. Calculations for initial  $^{87}\text{Sr}/^{86}\text{Sr}$  and  $\epsilon_{\text{Nd}(t)}$  show that the HSGs have  $^{87}\text{Sr}/^{86}\text{Sr}_i = 0.7082$  to 0.7123 and  $\epsilon_{\text{Nd}(t)} = -7.9$  to  $-8.9$ . The andesite samples define a range of  $^{87}\text{Sr}/^{86}\text{Sr}_i$  ratios from 0.7092 to 0.7096 and a range of  $\epsilon_{\text{Nd}(t)}$  from  $-7.2$  to  $-7.7$ . The dacites have  $^{87}\text{Sr}/^{86}\text{Sr}_i$  ratios that vary from 0.7097 to 0.7109 and  $\epsilon_{\text{Nd}(t)}$  values from  $-7.9$  to  $-8.0$ .

### Mineral chemistry

Clinopyroxene within the andesites exhibits a limited compositional range. Most samples contain augite, although some are more diopsidic, with compositions in the range  $\text{Wo}_{41\text{--}49}\text{En}_{39\text{--}44}\text{Fs}_{11\text{--}17}$  (Supplemental<sup>1</sup> Table S4). There is no significant difference in clinopyroxene compositions between the glomerocrysts (Supplemental<sup>1</sup> Figs. S1c and S1d;  $\text{Wo}_{41\text{--}49}\text{En}_{39\text{--}44}\text{Fs}_{12\text{--}17}$ ;  $\text{Mg}\# = 68\text{--}74$ ; where  $\text{Mg}\# = \text{atomic Mg}/[\text{Mg} + \text{Fe}_{\text{total}}]$ ) and discrete phenocrysts (Supplemental<sup>1</sup> Fig. S1e;  $\text{Wo}_{42\text{--}46}\text{En}_{40\text{--}44}\text{Fs}_{11\text{--}16}$ ;  $\text{Mg}\# = 69\text{--}75$ ). All clinopyroxene grains have relatively low trace-element concentrations (e.g., Sr = 29.2–40.9 ppm, Y = 18.8–37.9 ppm, Zr = 21.1–61.9 ppm, and V = 243–424 ppm) and exhibit weak Eu anomalies ( $\text{Eu}/\text{Eu}^* = 0.72\text{--}0.88$ ).

Within the Narusongduo andesites, amphiboles in the amphibole–quartz aggregates (Fig. 4a) display a narrow range in  $\text{SiO}_2$  (45.1–47.7 wt%) and  $\text{Al}_2\text{O}_3$  (5.56–6.33 wt%) concentrations (Supplemental<sup>1</sup> Table S5) and are characterized by a limited range in Ti (0.14 to 0.17 atoms per formula unit; apfu),  $\text{Al}_{\text{total}}$  (0.98 to 1.11 apfu), and alkali contents ( $\text{Na} + \text{K} = 0.80$  to 0.90 apfu). Values of  $\text{Mg}\#$  are between 63 and 67. Most amphiboles are edenite (Fig. 4b), with relatively high concentrations of some trace elements (e.g., Rb = 10.2–12.9 ppm, Y = 87.6–138 ppm, Zr = 219–367 ppm, and Zn = 115–138 ppm) and pronounced negative Eu anomalies ( $\text{Eu}/\text{Eu}^* = 0.13\text{--}0.17$ ).

Plagioclase is a major phase in the Narusongduo andesites. Aside from any compositional zoning within individual grains, plagioclase has An contents varying from  $\text{An}_{42}$  to  $\text{An}_{71}$ , with trace-element concentrations including 1211–1321 ppm Sr and 184–412 ppm Ba (Supplemental<sup>1</sup> Tables S6 and S7). The Ab–An exchange coefficient  $K_{\text{D}}(\text{An}–\text{Ab})^{\text{plagioclase}–\text{liquid}}$  varies from 0.15 to 0.48, suggesting equilibrium with whole-rock compositions.

### Pre-eruptive intensive parameters of the andesites

The pressure ( $P$ ) and temperature ( $T$ ) of crystallization and the water contents of the magmas of the andesites were calculated using a clinopyroxene–liquid thermobarometer (Neave

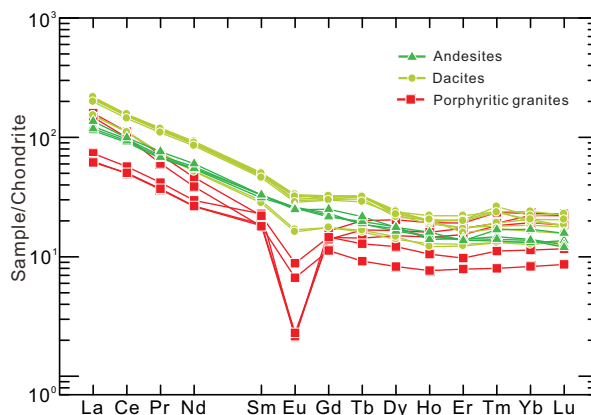


**FIGURE 3.** Chondrite-normalized REE patterns for the Narusongduo HSGs, andesites, and dacites. Normalizing values are from Sun and McDonough (1989). (Color online.)

and Putirka 2017) and a plagioclase–liquid hygrometer (Waters and Lange 2015), using the average whole-rock composition as the melt composition. The comparison between predicted and observed clinopyroxene components was used as a test of equilibrium between clinopyroxene and liquid (Fig. 5a; Mollo et al. 2013). Pressures recorded by clinopyroxene range between 1.0 and 4.3 kbar, with an average of  $2.2 \pm 0.8$  kbar; Fig. 5b), corresponding to depths of  $\sim 8$  km (assuming an average crustal density of  $2.8 \text{ g/cm}^3$ ). Corresponding temperatures range between 1023 and 1062 °C, with a mean of  $1036 \pm 8.4$  °C (Fig. 5b). Plagioclase crystals coexisting with clinopyroxene crystals were selected for estimation of initial magmatic water contents, and clinopyroxene  $P$ – $T$  was input into plagioclase–liquid hygrometer, similar to the application in Zhou et al. (2020a). It gives melt water concentrations that range between  $\sim 3.0\text{--}3.4$  wt%.

## DISCUSSION

### Evolution of the Narusongduo magmatic system

On the basis of our stratigraphic investigations, the eruptive sequence in the Narusongduo volcanic complex is summarized in Figure 1b and comprises (from old to young) (1) pyroclastic deposits, (2) dacitic volcanic rocks, (3) thick pyroclastic deposits, and (4) andesitic volcanic rocks. This sequence is consistent with geochronological results (Fig. 2).

Concordant U–Pb data from igneous zircon is generally interpreted to date crystallization of igneous rocks, assuming that all analyzed zircon crystals precipitated from their host magmas. However, there has been an increasing emphasis on the different origins of zircon crystals (Bacon and Lowenstern 2005; Miller et al. 2007) and multiple growth history of a single grain (e.g., Klemetti et al. 2011). Here, we use the criteria of Miller et al. (2007) to subdivide the zircon populations. The dacitic lavas erupted at an early stage, with zircon U–Pb dating on one sample (NR18-2-1) yielding a weighted mean age of  $65.4 \pm 0.4$  Ma (MSWD = 0.87; Fig. 2). Application of the Unmix Ages algorithm of Sambridge and Compston (1994) was not able to distinguish separate age components in this sample, suggesting that most of the analyzed zircons are autocrysts. Three andesite

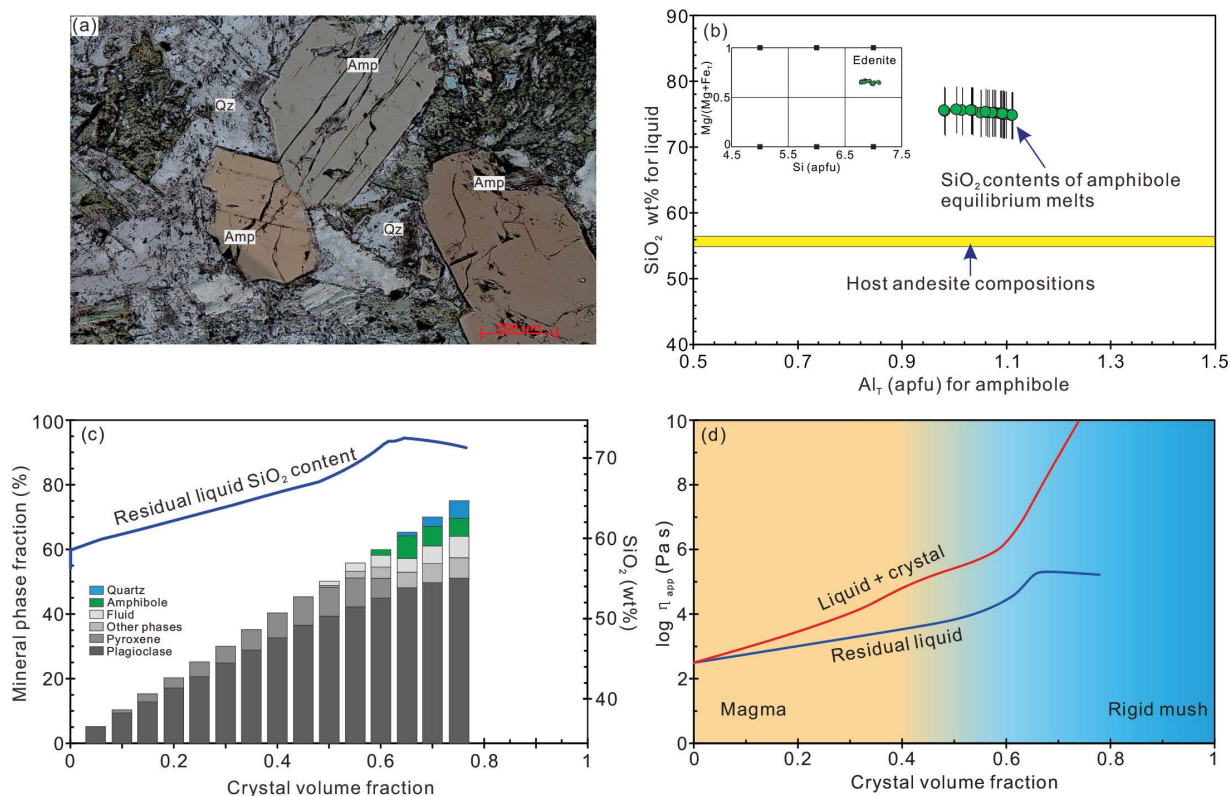


**FIGURE 4.** Conditions of amphibole crystallization and rigid storage of the Narusongduo andesite. (a) Photomicrograph of an amphibole–quartz glomerocryst in andesite. Amp = amphibole; Qz = quartz. (b) Relationship between amphibole composition and the SiO<sub>2</sub> content of coexisting liquid. The composition of the host andesite is denoted by the yellow bar. (c) Results of rhyolite-MELTS modeling of the Narusongduo andesite, showing mineral volume fraction and residual liquid SiO<sub>2</sub> content. (d) Changes in relative viscosity as a function of crystal volume fraction of the Narusongduo andesitic magma. The blue curve shows the viscosity of the residual liquid. The red curve represents the viscosity of magmas containing solid suspended particles. Amphibole crystallization starts when the system reaches a crystallinity of ~60 vol%, where rheological lock-up occurs. The detailed methods of rhyolite-MELTS and rheological modeling are presented in Supplemental Materials<sup>1</sup>. (Color online.)

samples yield near-identical younger ages of  $63.4 \pm 1.1$ ,  $63.2 \pm 0.6$ , and  $63.3 \pm 1.1$  Ma (Fig. 2b). These zircon crystals are also interpreted as autocrysts, and their ages likely represent the age of zirconium saturation, which regularly predate the eruption age by thousands to tens of thousands of years (e.g., Klemetti and Clyne 2014). However, older zircon populations are recognized in two of the andesite samples, one of which has an age of  $69.3 \pm 0.9$  Ma (NR18-4-1) and another an age of  $66.5 \pm 1.5$  Ma (NP2-15). The younger age is identical to the age of the dacites within analytical uncertainty, suggesting that these zircon grains can also be interpreted as antecrysts that crystallized within an earlier pulse. Whether the older population ( $69.3 \pm 0.9$  Ma) represents an earlier magma pulse or is genetically unrelated is unclear.

One sample of HSG (NR18-1-1) shows evidence for the presence of zircon antecrysts based on textural criteria (Supplemental<sup>1</sup> Fig. S2), whereas age components cannot be distinguished due to limited precision of SIMS analysis. The three samples of HSG yield different crystallization ages of  $61.7 \pm 0.6$ ,  $62.6 \pm 0.8$ , and  $62.7 \pm 0.4$  Ma, and the two of them have antecrystic ages of  $66.6 \pm 1.2$  and  $66.9 \pm 1.6$  Ma, respectively (Fig. 2). They were collected from different outcrops (Fig. 1b), implying that not all HSG plutons were emplaced simultane-

ously. Overall, our results suggest that magmatic activity in the Narusongduo system started at 65.4 Ma or earlier and ended by 61.7 Ma, with a total duration of at least 3.7 Myr.

Whole-rock isotopic compositions also yield important information regarding the evolution of magmatic systems. All magmatic suites within the Narusongduo volcanic complex have highly radiogenic Sr-Nd isotopic compositions (Supplemental<sup>1</sup> Table S3). Such evolved isotopic signatures indicate a significant contribution of crustal material to the magmatic system, consistent with previous studies that have revealed the presence of an ancient crustal basement beneath the northern Gangdese batholith (Zhu et al. 2011; Hou et al. 2015). Owing to the high Rb/Sr ratios of the HSGs and potential modification of strontium isotopes by alteration, we restrict our discussion to the neodymium isotopic compositions. Although most of the igneous suites have similar crustal isotopic signatures, a systematic variation can be identified. Epsilon Nd values increases from the andesites to the HSGs, and most of the HSG samples are nearly located on the line of the combined assimilation and fractional crystallization (AFC), with an  $r$  value of 0.1, where  $r = m_a/m_c$  ( $m_a$  represents the mass fraction of assimilated material and  $m_c$  is the amount of crystallized material, assuming the average andesite composition

as the parental melt composition and an ancient crust-derived melts (represented by the ancient granites in the Gangdese arc, Zhang et al. 2012) is being assimilated (Supplemental<sup>1</sup> Fig. S3). Given the similarity in age between the andesites and HSGs, and the presence of abundant zircon antecrysts, it cannot be ruled out that the HSGs may represent evolved compositions derived from the andesitic magmas. Further discussion is provided in the following parts.

### The presence of an andesitic magma reservoir within the upper crust

The andesitic lavas are the youngest eruptive products in the Narusongduo volcanic complex and show a close temporal relationship with the HSGs (Figs. 1b and 2). Consequently, we focus our petrologic reconstruction on the magmatic plumbing system that fed the andesitic eruptions. Amphibole major and trace element compositions have been utilized to decipher magmatic processes and conditions of crystallization (e.g., Putirka 2016; Barnes et al. 2016; Zhou et al. 2020b), and the SiO<sub>2</sub> content in coexisting liquids can be estimated reliably using only amphibole chemistry (Ridolfi et al. 2010; Ridolfi and Renzulli 2012; Erdmann et al. 2014; Zhang et al. 2017; Humphreys et al. 2019). Amphibole in the crystal aggregates (Fig. 4a) within the andesites have Si atoms of 6.8 to 7.1 per 23 O atoms, and they are crystallized from high-silica melts (74.8–75.7 wt% SiO<sub>2</sub>; Fig. 4b) using the equations presented by Putirka (2016). This scenario can be predicted approximately by the rhyolite-MELTS modeling (Gualda et al. 2012; Gualda and Ghiorso 2015), using the average whole-rock composition as a starting melt. The results suggest that amphibole crystallization begins when residual liquid SiO<sub>2</sub> contents exceed 70 wt% (Fig. 4c). It is noteworthy that the phase assemblages from rhyolite-MELTS modeling here should be treated with caution because rhyolite-MELTS cannot easily deal with amphibole crystallization (Ghiorso and Sack 1995; Gualda et al. 2012). However, the situation that amphibole crystallizes from more evolved melts than the bulk-rock composition of the host is consistent with general observations in plutonic rocks (e.g., Werts et al. 2020), as well as the observed coexistence of amphibole and quartz within some glomerocrysts in this study (Fig. 4a; Supplemental Fig. S1f).

These constraints on amphibole crystallization have important implications for the pre-eruptive state of the andesitic magmas. In the Narusongduo andesitic magmas, amphibole becomes saturated when the system reaches a crystallinity of ~60 vol% (Fig. 4c). Although an increase in the volume of bubbles due to fluid saturation can decrease the residual melt viscosity (Figs. 4c and 4d), non-Newtonian behavior induces an increase in the bulk viscosity of magmas (crystals plus melts plus bubbles) by several orders of magnitude (Caricchi et al. 2007) when the crystallinity rises above ~60 vol% (Fig. 4d). Such high viscosity leads to a transition from active magmas to a rheologically locked crystal mush (e.g., Costa et al. 2009; Sparks and Cashman 2017). Combined with the results from clinopyroxene–liquid thermobarometry, these data provide evidence supporting the presence of an andesitic magma reservoir in the upper crust, at a depth of about 8 km, consistent with thermo-mechanical modeling results concerning the optimal depth of subvolcanic magma accumulation (e.g., Huber et al. 2019).

Although reverse-zoned crystals are commonly interpreted as a record of pre-eruptive recharge of a magma reservoir (e.g., Murphy et al. 2000), complex phenocryst textures can also be ascribed to decompression-driven crystallization (e.g., Crabbtree and Lange 2011), with no requirement for magma recharge. Changes in the liquid composition may distinguish between these two processes: decompression-driven crystallization will lead to compositions evolving along the liquid line of descent, whereas magma recharge may produce the opposite trend. Liquid compositions calculated using plagioclase trace-element compositions and equilibrium partition data depend mainly on An content and temperature (e.g., Bindeman et al. 1998). Calculations indicate that the liquids in equilibrium with reverse-zoned plagioclase crystals in the andesites had average Mg contents increasing from 0.73 to 1.35 wt% (at 1000 °C) from core to rim (Fig. 6). Mg is a mobile element in plagioclase at magmatic temperatures (e.g., Van Orman et al. 2014; Fabbro et al. 2017), and the effects of subsequent diffusion cannot be ignored. However, the liquids in equilibrium with the Mg concentrations measured in the core do not overlap with those calculated to be in equilibrium with the rim (Fig. 6), suggesting that the initial zoning in Mg was not destroyed completely by diffusion. This MgO distribution is the

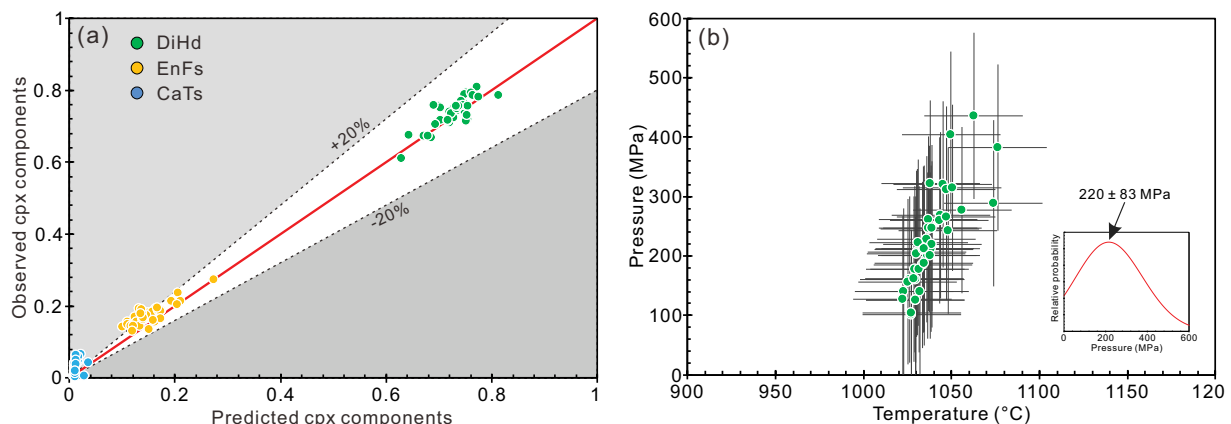


**FIGURE 5.** (a) Comparison between predicted and observed clinopyroxene components as a test of clinopyroxene–liquid equilibrium (Mollo et al. 2013). (b) *P*-*T* estimates for the Narusongduo andesites based on the clinopyroxene–liquid thermobarometry (Neave and Putirka 2017). (Color online.)

opposite of the liquid line of descent, and an abrupt change in the liquid composition (Fig. 6) is more likely to be caused by mixing following magma recharge (Supplemental<sup>1</sup> Fig. S4). Thus, the reverse-zoned plagioclases in the Narusongduo andesites are also consistent with the presence of an andesitic magma reservoir.

**Constraining the magma reservoir evolution using trace-element systematics**

The Narusongduo HSGs are characterized by pronounced negative Eu anomalies ( $Eu/Eu^* = 0.11\text{--}0.47$ ) and low Zr/Hf values ( $22.5\text{--}37.0$ ). In the andesitic magma reservoir, the evolution of  $Eu/Eu^*$  can be constrained by considering clinopyroxene and amphibole compositions, as the clinopyroxenes record near-liquidus temperatures ( $1023\text{ to }1063\text{ }^\circ\text{C}$ ), whereas the amphiboles crystallized at near-solidus temperatures ( $798\text{ to }841\text{ }^\circ\text{C}$ ). Here, a lattice strain model was used for estimating the mineral/melt

partition coefficients of clinopyroxene and amphibole (Blundy and Wood 1994), for which the lattice strain parameters were obtained by parameterized models based on mineral compositions (Wood and Blundy 1997; Hill et al. 2011; Shimizu et al. 2017). The calculated partition coefficients for REEs for the clinopyroxenes and amphiboles were employed to calculate REE, Zr, and Hf concentrations of the melts from which the clinopyroxenes and amphiboles crystallized. As illustrated in Figure 7a, clinopyroxene equilibrium melts display weak Eu anomalies ( $Eu/Eu^* = 0.72\text{--}0.88$ ), but amphibole equilibrium melts have pronounced negative Eu anomalies ( $Eu/Eu^* = 0.13\text{--}0.17$ ). Combined with their crystallization temperatures, we would expect that evolved residual melts developed increasingly pronounced negative Eu anomalies with progressive crystallization of the andesitic magma reservoir.

Zirconium saturation in magmas is dependent on temperature,

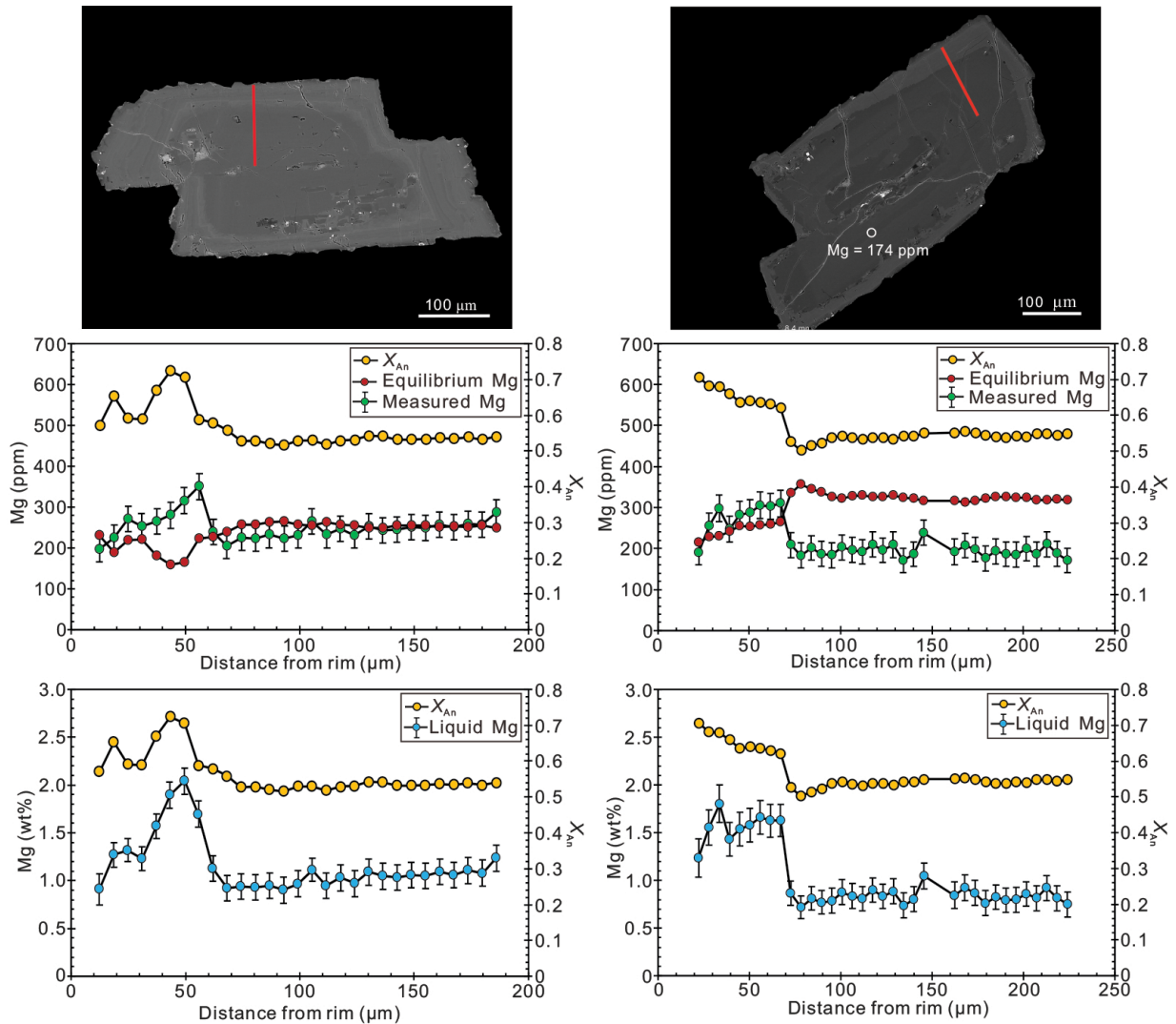


**FIGURE 6.** Backscattered electron images, compositional profiles for selected plagioclase grains, and calculated liquid compositions. The profiles for Mg content (green spots) were calculated to be in equilibrium with liquid, which is in equilibrium with the crystal rim, using published An-dependent partition coefficients (Bindeman et al. 1998) at  $1000\text{ }^\circ\text{C}$ . A spot (a white circle in BSE image) whose Mg content was determined using LA-ICP-MS is also shown for comparison. Further details are contained in Supplemental Materials, and the data are presented in Supplemental<sup>1</sup> Table S6. (Color online.)



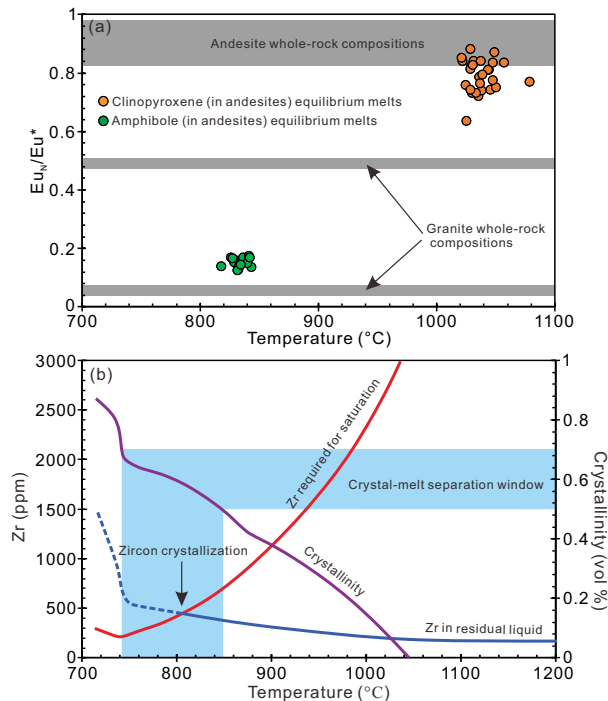


**FIGURE 7.** (a)  $Eu/Eu^*$  vs. temperature. Using compositions of amphibole and clinopyroxene (from the andesites), equilibrium melts were calculated using our predicted partition coefficients. The whole-rock compositions of the HSGs and andesites are shown by the gray bars. (b) Zr saturation modeling for the Narusongduo andesites. The Zr content of the residual liquid throughout the crystallization interval was calculated using bulk partition coefficients for the saturated phases as predicted by rhyolite-MELTS modeling. The zircon solubility model of Boehnke et al. (2013) was employed to calculate the Zr concentration required for saturation of the evolving liquid. The window for efficient crystal–liquid separation is denoted by the blue region (Dufek and Bachmann 2010). (Color online.)

the Zr content of the melt, and the parameter  $M$ , where  $M = [(Na + K + 2Ca)/(Al \times Si)]$  (Boehnke et al. 2013). Residual melt Zr contents can be calculated throughout the crystallization interval using bulk partition coefficients (see Supplemental Materials<sup>1</sup>) for the saturated phases as predicted by calculations using rhyolite-MELTS (Fig. 4c). The major-element compositions of the residual liquids were used to determine the  $M$  parameter, and the zircon solubility model of Boehnke et al. (2013) was then employed to calculate the Zr concentration required for zircon crystallization. As shown in Figure 7b, temperatures for zircon crystallization in the Narusongduo andesites are  $\sim 800^{\circ}C$ , and the window for crystal–liquid separation extends from 742 to 848  $^{\circ}C$ , suggesting low Zr/Hf ratios of some HSGs can be ascribed to zircon fractionation (e.g., Claiborne et al. 2006; Linnen and Keppler 2002).

#### Extraction of HSGs from the shallow andesitic magma reservoir

We propose that the Narusongduo HSGs represent melts extracted from the shallow andesitic magma reservoir, on the basis of several lines of evidence. First, the close temporal relationship

between the HSGs and andesites. Second, the Narusongduo HSGs contain abundant zircon antecrysts. Third, most HSGs show pronounced negative Eu anomalies (Fig. 3), consistent with highly evolved melts that were derived from the andesitic magma reservoir, as recorded by the amphiboles in the andesites (Fig. 7a). Fourth, the Narusongduo HSGs have low Zr/Hf ratios (average Zr/Hf = 28.4), which is a relatively robust proxy for identifying highly evolved magmas that were extracted from zircon-saturated mush zones (Linnen and Keppler 2002; Bea et al. 2006; Claiborne et al. 2006; Deering and Bachmann 2010; Deering et al. 2016; Wu et al. 2017). The samples of HSG have variable Zr/Hf ratios varying from 22 to 37, suggesting either that they were extracted from the andesitic magma reservoir at different cycles or that they were derived from disconnected melt lenses (e.g., Till et al. 2019) with variable proportions of cumulate zircon, consistent with the diverse ages of zircon antecrysts (Fig. 2). If the separation of melt-rich lenses occurred after zircon crystallization (Fig. 7b), then the extracted melts would have significantly lower Zr/Hf ratios, such as the HSG samples with Zr/Hf = 22–24.

The mechanisms for crystal–melt separation at shallow crustal levels are debated (e.g., Lee and Morton 2015; Holness 2018; Bachmann and Huber 2019). In the cold upper crust, heat is a critical factor in determining the behavior of shallow magmatic systems (e.g., Blundy and Annen 2016). The capability for phase separation in upper-crustal magma reservoirs therefore depends on several factors, such as the timescale for concentrating intergranular melts and the longevity of magma bodies above their solidus. If active over several million years, a transcrustal magmatic system can modify the crustal geotherm, leading to the formation of shallow-crustal magma reservoirs with enhanced survivability (e.g., Karakas et al. 2017), ultimately providing sufficient time for crystal–melt separation (Bachmann and Huber 2019). Magmatism in the Narusongduo system lasted at least  $\sim 3.7$  Myr with or without lulls during which emplacement of HSGs occurred only in the latter stages. This progression from lower to higher silica magmas over millions of years timescale has also been observed in other plutonic or volcanic systems (e.g., Glazner et al. 2004; Grunder et al. 2008).

The importance of water to the segregation of  $SiO_2$ -rich melts is widely recognized (e.g., Lee et al. 2015; Hartung et al. 2019). Amphiboles within the crystal aggregates (Fig. 4a) from the andesites studied here have high fluorine contents ( $2.17 \pm 0.18$  wt%; Supplemental<sup>1</sup> Table S5), and these amphiboles have been interpreted as a record of highly evolved melts of the magma reservoir (Fig. 4b). Then we can expect that melt-rich lenses in the magma reservoir should be characterized by high fluorine concentrations. Dissolved F can decrease the density and viscosity of melt (Fig. 8), lower solidus temperatures, and increase the solubility of  $H_2O$  (e.g., Holtz et al. 1993; Giordano et al. 2004; Baasner et al. 2013). More importantly, unlike other volatiles such as  $H_2O$ , F has a high solubility in  $SiO_2$ -rich melts at low pressure (Giordano et al. 2004). Consequently, crystal–melt separation in shallow magma reservoirs should be facilitated by the presence of F, consistent with the observation that F is abundant in many highly evolved granites and rhyolites (e.g., Giordano et al. 2004; Audétat 2015). In addition, we examined quartz phenocrysts hosted in the Narusongduo HSGs using CL

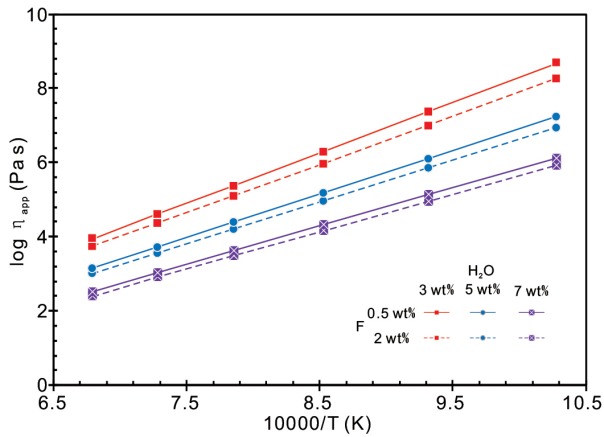


**FIGURE 8.** Comparison of melt viscosities using the average composition of the Narusongduo HSGs with different H<sub>2</sub>O and F contents. The viscosity model of Giordano et al. (2008) was employed. (Color online.)

imaging. Quartz CL brightness tends to correlate with Ti concentration in igneous quartz (Matthews et al. 2012), and CL grayscale (a numerical value assigned to brightness) values can be used as a proxy for Ti concentration in quartz (Matthews et al. 2012) as well as temperature variations during crystal growth history (Wark and Waston 2006). CL imaging reveals that some quartz phenocrysts in the Narusongduo HSGs exhibit distinct growth zonation, with low-intensity CL cores overgrown by high-intensity CL rims (Fig. 9a). The three-dimensional effect of CL grayscale values is presented in Figure 9b using the MATLAB program. The major step in CL brightness toward the crystal rims provides evidence for a magma reservoir recharge event resulting in the elevation of temperature (Wark et al. 2007). Magma recharge is likely an efficient mechanism triggering magma ascent by lowering magma density in response to an injection of volatiles or temperature increase (e.g., Snyder 2000). Thus, we infer that the underplating of a hotter magma to the high-silica liquid cap of the magma reservoir promoted the melt extraction (Fig. 10).

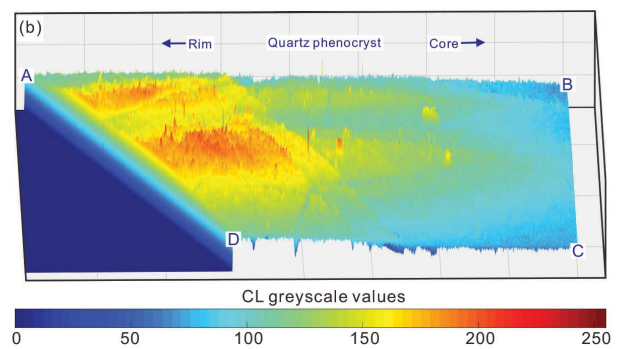
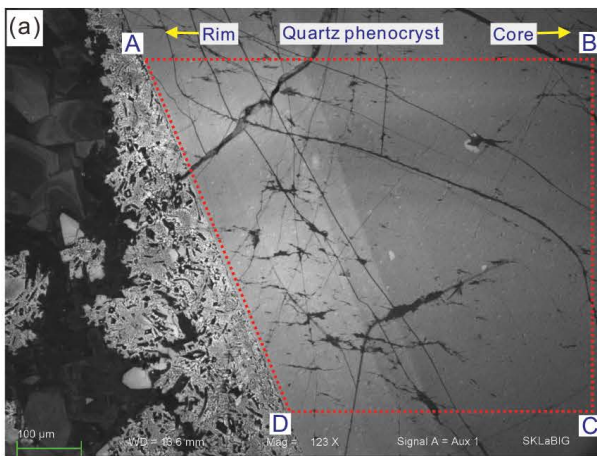


**FIGURE 9.** CL and 3D grayscale image of selected quartz crystal from the Narusongduo HSGs. Panel (a) shows the quartz phenocryst have distinct growth zonation with low-intensity CL cores overgrown by a high-intensity CL rim, and granophyric intergrowths of quartz and alkali-feldspar in the groundmass. Markers (A, B, C, and D) in a correspond with the locations in b. (Color online.)

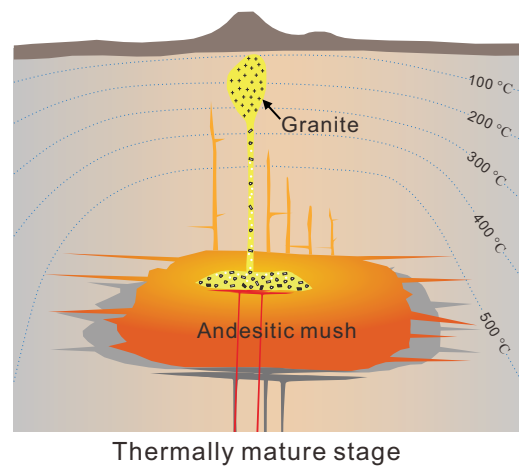
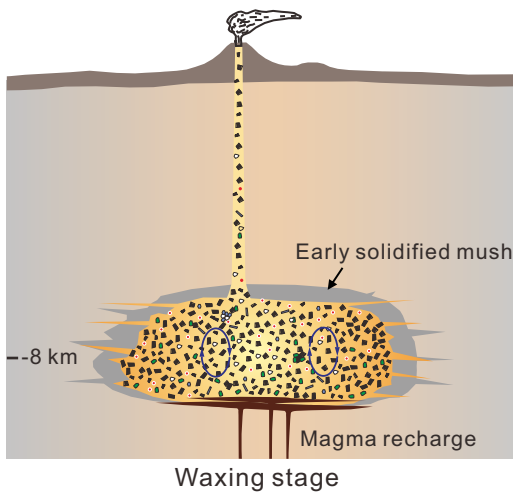


**FIGURE 10.** Schematic cross-section showing a model for emplacement of the Narusongduo HSGs. After a long period of magmatic activity (>3.7 Myr), the upper crust became thermally mature, enhancing the survivability of the intermediate magma reservoir. Evolved high-silica melts then segregated and ascended to form HSGs. The thermal structure of the upper crust after a long period of magmatic activity is modified from the modeling results by Karakas et al. (2019). (Color online.)

## IMPLICATIONS

Identification of the field examples that pluton-scale high-silica granites represent melts extracted from upper-crustal magma reservoirs is critical for understanding the behavior of shallow magmatic systems. This study provides an excellent example of kilometer-scale HSG bodies that formed through crystal–melt separation at shallow crustal levels. Our results indicate that the Narusongduo magmatic system was constructed over  $\geq 3.7$  Myr with or without lulls, and the formation of the andesitic magma reservoir (at a paleodepth of  $\sim 8$  km) as well as the emplacement of HSGs occurred during the late, thermally mature stage. It contributes to a broad range of issues concerning silicic magmatism such as the behaviors of shallow magmatic systems, the volcanic–plutonic connections, and particularly for currently hot debates on the capability and efficiency of crystal–melt separation in upper crustal magma reservoirs (e.g., Bachmann and Huber 2019). In addition, one of the most destructive kinds of volcanic hazards on Earth is the eruptions of high-SiO<sub>2</sub>, viscous rhyolites. Dynamic processes of the emplacement of high-silica granites in this study are similar to those of high-SiO<sub>2</sub> rhyolites and likely represent failed eruptions of rhyolites, then an important question arises that why some highly evolved melts erupted and others failed, which may require a comprehensive approach on better deciphering the physical processes.

## ACKNOWLEDGMENTS

We thank Gareth Fabbro for discussions on equilibrium liquid calculation and Mg diffusion in plagioclase. We appreciate Ya-Nan Yang, Qing Yang, Le Zhang, Peng-Li He, Fan Yang, and Peng-Fei Ma for laboratory assistance, as well as Ying-Chao Liu, Zhen-Qing Li, Qi-Wei Li, Tong-Yu Huang, Xiao-Yan Zhao, Fan Fei, Xiong Zhang, and Yu-Tao Xu for extensive help on geologic mapping and stratigraphic investigation in the field. We are grateful to Calvin Barnes, Erik Klemetti, and an anonymous reviewer for helpful, constructive reviews and Chad Deering for comments on early versions.

## FUNDING

This research was supported in part by the National Key Research and Development Program of China “Deep Structure and Ore-forming Process of Main Mineralization System in Tibetan Orogen” (2016YFC0600306) to Z.S. Yang; the Second Tibetan Plateau Scientific Expedition and Research (STEP) (2019QZKK0702), the National Natural Science Foundation of China (9185215 and 41630208), the Strategic Priority Research Program (A) of the Chinese Academy of Sciences (grant no. XDA2007030402), and the Guangzhou Institute of Geochemistry, Chinese Academy of Science (GIGCAS 135 project (135TP201601) to Q. Wang; the National Natural Science Foundation of China (41802061) to J.S. Zhou.

## REFERENCES CITED

- Annen, C., Blundy, J.D., and Sparks, R.S.J. (2006) The genesis of intermediate and silicic magmas in deep crustal hot zones. *Journal of Petrology*, 47, 505–539.
- Audétat, A. (2015) Compositional evolution and formation conditions of magmas and fluids related to porphyry Mo mineralization at Climax, Colorado. *Journal of Petrology*, 56, 1519–1546.
- Baasner, A., Schmidt, B.C., and Webb, S.L. (2013) The effect of chlorine, fluorine and water on the viscosity of aluminosilicate melts. *Chemical Geology*, 357, 134–149.
- Bachmann, O., and Bergantz, G.W. (2004) On the origin of crystal–poor rhyolites: Extracted from batholithic crystal mushes. *Journal of Petrology*, 45, 1565–1582.
- Bachmann, O., and Huber, C. (2019) The inner workings of crustal distillation columns; the physical mechanisms and rates controlling phase separation in silicic magma reservoirs. *Journal of Petrology*, 60, 3–18.
- Bacon, C.R., and Lowenstern, J.B. (2005) Late Pleistocene granodiorite source for recycled zircon and phenocrysts in rhyodacite lava at Crater Lake, Oregon. *Earth and Planetary Science Letters*, 233, 277–293.
- Barnes, C.G. (1983) Petrology and upward zonation of the Wooley Creek batholith, Klamath Mountains, California. *Journal of Petrology*, 24, 495–537.
- Barnes, C.G., Memeti, V., and Coint, N. (2016) Deciphering magmatic processes in calc–alkaline plutons using trace element zoning in hornblende. *American Mineralogist*, 101, 328–342.
- Bateman, P.C., and Chappell, B.W. (1979) Crystallization, fractionation, and solidification of the Tuolumne intrusive series, Yosemite National Park, California. *Geological Society of America Bulletin*, 90, 465–482.
- Bea, F., Montero, P., and Ortega, M. (2006) A LA–ICP–MS evaluation of Zr reservoirs in common crustal rocks: implications for Zr and Hf geochemistry, and zircon-forming processes. *Canadian Mineralogist*, 44, 693–714.
- Bindeman, I.N., Davis, A.M., and Drake, M.J. (1998) Ion microprobe study of plagioclase–basalt partition experiments at natural concentration levels of trace elements. *Geochimica et Cosmochimica Acta*, 62, 1175–1193.
- Blundy, J.D., and Annen, C.J. (2016) Crustal magmatic systems from the perspective of heat transfer. *Elements*, 12, 115–120.
- Blundy, J., and Wood, B. (1994) Prediction of crystal–melt partition coefficients from elastic moduli. *Nature*, 372, 452–454.
- Boehnke, P., Watson, E.B., Trail, D., Harrison, T.M., and Schmitt, A.K. (2013) Zircon saturation re-visited. *Chemical Geology*, 351, 324–334.
- Caricchi, L., and Blundy, J. (2015) The temporal evolution of chemical and physical properties of magmatic systems. *Geological Society, London, Special Publications*, 422, 1–15.
- Caricchi, L., Burlini, L., Ulmer, P., Gerya, T., Vassalli, M., and Papale, P. (2007) Non-Newtonian rheology of crystal-bearing magmas and implications for magma ascent dynamics. *Earth and Planetary Science Letters*, 264, 402–419.
- Chung, S.L., Chu, M.F., Zhang, Y., Xie, Y., Lo, C.H., and Lee, T.Y. (2005) Tibetan tectonic evolution inferred from spatial and temporal variations in post-collisional magmatism. *Earth Science Reviews*, 68, 173–196.
- Claiborne, L.L., Miller, C.F., Walker, B.A., Wooden, J.L., Mazdab, F.K., and Bea, F. (2006) Tracking magmatic processes through Zr/Hf ratios in rocks and Hf and Ti zoning in zircons: an example from the Spirit Mountain batholith, Nevada. *Mineralogical Magazine*, 70, 517–543.
- Clemens, J.D., and Stevens, G. (2012) What controls chemical variation in granitic magmas? *Lithos*, 134–135, 317–329.
- Coleman, D.S., Bartley, J.M., Glazner, A.F., and Pardue, M.J. (2012) Is chemical zonation in plutonic rocks driven by changes in source magma composition or shallow-crustal differentiation? *Geosphere*, 8, 1568–1587.
- Costa, A., Caricchi, L., and Bagdassarov, N. (2009) A model for the rheology of particle-bearing suspensions and partially molten rocks. *Geochimica, Geophysics, Geosystems*, 10, N3.
- Crabtree, S.M., and Lange, R.A. (2011) Complex phenocryst textures and zoning patterns in andesites and dacites: evidence of degassing-induced rapid crystallization? *Journal of Petrology*, 52, 3–38.
- de Silva, S.L., and Gregg, P.M. (2014) Thermomechanical feedbacks in magmatic systems: Implications for growth, longevity, and evolution of large caldera-forming magma reservoirs and their supereruptions. *Journal of Volcanology and Geothermal Research*, 282, 77–91.
- Deering, C.D., and Bachmann, O. (2010) Trace element indicators of crystal accumulation in silicic igneous rocks. *Earth and Planetary Science Letters*, 297, 324–331.
- Deering, C.D., Cole, J.W., and Vogel, T.A. (2011) Extraction of crystal-poor rhyolite from a hornblende-bearing intermediate mush: a case study of the caldera-forming Matahina eruption, Okataina volcanic complex. *Contributions to Mineralogy and Petrology*, 161, 129–151.
- Deering, C.D., Keller, B., Schoene, B., Bachmann, O., Beane, R., and Ovtcharova, M. (2016) Zircon record of the plutonic–volcanic connection and protracted rhyolite melt evolution. *Geology*, 44, 267–270.
- Dufek, J., and Bachmann, O. (2010) Quantum magmatism: Magmatic compositional gaps generated by melt–crystal dynamics. *Geology*, 38, 687–690.
- Erdmann, S., Martel, C., Pichavant, M., and Kushnir, A. (2014) Amphibole as an archivist of magmatic crystallization conditions: Problems, potential, and implications for inferring magma storage prior to the paroxysmal 2010 eruption of Mount Merapi, Indonesia. *Contributions to Mineralogy and Petrology*, 167, 1016–1038.
- Fabbro, G.N., Druitt, T.H., and Costa, F. (2017) Storage and eruption of silicic magma across the transition from dominantly effusive to caldera-forming states at an arc volcano (Santorini, Greece). *Journal of Petrology*, 58, 2429–2464.
- Ghiorso, M.S., and Sack, R.O. (1995) Chemical mass transfer in magmatic processes IV. A revised and internally consistent thermodynamic model for the interpolation and extrapolation of liquid–solid equilibria in magmatic systems at elevated temperatures and pressures. *Contributions to Mineralogy and Petrology*, 119, 197–212.
- Giordano, D., Romano, C., Dingwell, D.B., Poe, B., and Behrens, H. (2004) The combined effects of water and fluorine on the viscosity of silicic magmas. *Geochimica et Cosmochimica Acta*, 68, 5159–5168.
- Giordano, D., Russell, J.K., and Dingwell, D.B. (2008) Viscosity of magmatic liquids: a model. *Earth and Planetary Science Letters*, 271, 123–134.
- Glazner, A.F., Bartley, J.M., Coleman, D.S., Gray, W., and Taylor, R.Z. (2004) Are plutons assembled over millions of years by amalgamation from small magma chambers? *GSA Today*, 14, 4–12.
- Grunder, A.L., Klemetti, E.W., Feeley, T.C., and McKee, C.M. (2008) Eleven million years of arc volcanism at the Aucanquilcha Volcanic Cluster, northern Chilean Andes: implications for the life span and emplacement of plutons. *Earth and Environmental Science Transactions of the Royal Society of*

- Edinburgh, 97, 415–436.
- Gualda, G.A., and Ghiorso, M.S. (2015) MELTS\_Excel: A Microsoft Excel-based MELTS interface for research and teaching of magma properties and evolution. *Geochemistry, Geophysics, Geosystems*, 16, 315–324.
- Gualda, G.A.R., Ghiorso, M.S., Lemons, R.V., and Carley, T.L. (2012) Rhyolite-MELTS: A modified calibration of MELTS optimized for silica-rich, fluid-bearing magmatic systems. *Journal of Petrology*, 53, 875–890.
- Hartung, E., Weber, G., and Caricchi, L. (2019) The role of H<sub>2</sub>O on the extraction of melt from crystallising magmas. *Earth and Planetary Science Letters*, 508, 85–96.
- Hildreth, W. (1979) The Bishop Tuff: evidence for the origin of compositional zonation in silicic magma chambers. *Geological Society of America Special Paper*, 180, 43–75.
- (1981) Gradients in silicic magma chambers: Implications for lithospheric magmatism. *Journal of Geophysical Research: Solid Earth*, 86, 10153–10192.
- Hildreth, W., and Moorbath, S. (1988) Crustal contributions to arc magmatism in the Andes of central Chile. *Contributions to Mineralogy and Petrology*, 98, 455–489.
- Hill, E., Blundy, J.D., and Wood, B.J. (2011) Clinopyroxene-melt trace element partitioning and the development of a predictive model for HFSE and Sc. *Contributions to Mineralogy and Petrology*, 161, 423–438.
- Holness, M.B. (2018) Melt segregation from silicic crystal mushes: a critical appraisal of possible mechanisms and their microstructural record. *Contributions to Mineralogy and Petrology*, 173, 48.
- Holtz, F., Dingwell, D.B., and Behrens, H. (1993) Effects of F, B<sub>2</sub>O<sub>3</sub> and P<sub>2</sub>O<sub>5</sub> on the solubility of water in haplogranite melts compared to natural silicate melts. *Contributions to Mineralogy and Petrology*, 113, 492–501.
- Hou, Z.Q., Duan, L.F., Lu, Y.J., Zheng, Y.C., Zhu, D.C., Yang, Z.M., Yang, Z.S., Wang, B.D., Pei, Y.R., Zhao, Z.D., and McCuaig, C. (2015) Lithospheric architecture of the Lhasa Terrane and its control on ore deposits in the Himalayan-Tibetan Orogen. *Economic Geology*, 110, 1541–1575.
- Huber, C., Townsend, M., Degruyter, W., and Bachmann, O. (2019) Optimal depth of subvolcanic magma chamber growth controlled by volatiles and crust rheology. *Nature Geoscience*, 12, 762–768.
- Humphreys, M.C., Cooper, G.F., Zhang, J., Loewen, M., Kent, A.J., Macpherson, C.G., and Davidson, J.P. (2019) Unravelling the complexity of magma plumbing at Mount St. Helens: a new trace element partitioning scheme for amphibole. *Contributions to Mineralogy and Petrology*, 174, 9.
- Ji, W.Q., Wu, F.Y., Chung, S.L., Li, J.X., and Liu, C.Z. (2009) Zircon U-Pb geochronology and Hf isotopic constraints on petrogenesis of the Gangdese batholith, southern Tibet. *Chemical Geology*, 262, 229–245.
- Ji, X.H., Yang, Z.S., Yu, Y.S., Shen, J.F., Tian, S.H., Meng, X.J., Li, Z.Q., and Liu, Y.C. (2012) Formation mechanism of magmatic rocks in Narusongduo lead-zinc deposit of Tibet: Evidence from magmatic zircon. *Mineral Deposits*, 31, 758–774 (in Chinese with English abstract).
- Karakas, O., Degruyter, W., Bachmann, O., and Dufek, J. (2017) Lifetime and size of shallow magma bodies controlled by crustal-scale magmatism. *Nature Geoscience*, 10, 446–450.
- Karakas, O., Wotzlaw, J.F., Guillong, M., Ulmer, P., Brack, P., Economos, R., Bergantz, G.W., Sinigoi, S., and Bachmann, O. (2019) The pace of crustal-scale magma accretion and differentiation beneath silicic caldera volcanoes. *Geology*, 47, 719–723.
- Klemetti, E.W., and Clynne, M.A. (2014) Localized rejuvenation of a crystal mush recorded in zircon temporal and compositional variation at the Lassen Volcanic Center, Northern California. *PLoS ONE*, 9, e113157.
- Klemetti, E.W., Deering, C.D., Cooper, K.M., and Roeske, S.M. (2011) Magmatic perturbations in the Okataina Volcanic Complex, New Zealand at thousand-year timescales recorded in single zircon crystals. *Earth and Planetary Science Letters*, 305, 185–194.
- Lee, C.-T. A., and Morton, D.M. (2015) High silica granites: Terminal porosity and crystal settling in shallow magma chambers. *Earth and Planetary Science Letters*, 409, 23–31.
- Lee, C.T.A., Morton, D.M., Farnier, M.J., and Moitra, P. (2015) Field and model constraints on silicic melt segregation by compaction/hindered settling: The role of water and its effect on latent heat release. *American Mineralogist*, 100, 1762–1777.
- Li, X.H., Li, Z.X., Wingate, M.T.D., Chung, S.L., Liu, Y., Lin, G.C., and Li, W.X. (2006) Geochemistry of the 755 Ma Mundine Well dyke swarm, northwestern Australia: Part of a Neoproterozoic mantle superplume beneath Rodinia? *Precambrian Research*, 146, 1–15.
- Li, X.H., Liu, Y., Li, Q.L., Guo, C.H., and Chamberlain, K.R. (2009) Precise determination of Phanerozoic zircon Pb/Pb age by multicollector SIMS without external standardization. *Geochemistry, Geophysics, Geosystems*, 10, Q04010.
- Li, X.H., Tang, G.Q., Gong, B., Yang, Y.H., Hou, K.J., Hu, Z.C., Li, Q.L., Liu, Y., and Li, W.X. (2013) Qinghu zircon: a working reference for microbeam analysis of U-Pb age and Hf and O isotopes. *Chinese Science Bulletin*, 58, 4647–4654.
- Linnen, R.L., and Keppler, H. (2002) Melt composition control of Zr/Hf fractionation in magmatic processes. *Geochimica et Cosmochimica Acta*, 66, 3293–3301.
- Lipman, P.W. (1988) Evolution of silicic magma in the upper crust: The mid-Tertiary Latir volcanic field and its cogenetic granitic batholith, northern New Mexico, USA. *Earth and Environmental Science Transactions of The Royal Society of Edinburgh*, 79, 265–288.
- Ludwig, K.R. (2003) A geochronological toolkit for Microsoft Excel. Berkeley Geochronology Center. Special Publication no. 4, 71 pp.
- Ma, L., Wang, Q., Kerr, A.C., Yang, J.-H., Xia, X.-P., Quan, O., Yang, Z.-Y., and Sun, P. (2018) Paleocene (c. 62 Ma) Leucogranites in Southern Lhasa, Tibet: products of syn-collisional crustal anatexis during slab roll-back? *Journal of Petrology*, 58, 2089–2114.
- Matthews, N.E., Huber, C., Pyle, D.M., and Smith, V.C. (2012) Timescales of magma recharge and reactivation of large silicic systems from Ti diffusion in quartz. *Journal of Petrology*, 53, 1–32.
- Miller, C.F., and Miller, J.S. (2002) Contrasting stratified plutons exposed in tilt blocks, Eldorado Mountains, Colorado River Rift, NV, USA. *Lithos*, 61, 209–224.
- Miller, C.F., Watson, E.B., and Harrison, T.M. (1988) Perspectives on the source, segregation and transport of granitoid magmas. *Earth and Environmental Science Transactions of The Royal Society of Edinburgh*, 79, 135–156.
- Miller, J., Matzel, J., Miller, C., Burgess, S., and Miller, R. (2007) Zircon growth and recycling during the assembly of large, composite arc plutons. *Journal of Volcanology and Geothermal Research*, 167, 282–299.
- Mo, X., Niu, Y., Dong, G., Zhao, Z., Hou, Z., Zhou, S., and Ke, S. (2008) Contribution of syncollisional felsic magmatism to continental crust growth: a case study of the Paleogene Linzizong volcanic succession in southern Tibet. *Chemical Geology*, 250, 49–67.
- Mollo, S., Putirka, K., Misiti, V., Soligo, M., and Scarlato, P. (2013) A new test for equilibrium based on clinopyroxene-melt pairs: Clues on the solidification temperatures of Etruscan alkaline melts at post-eruptive conditions. *Chemical Geology*, 352, 92–100.
- Murphy, M.D., Sparks, R.S.J., Barclay, J., Carroll, M.R., and Brewer, T.S. (2000) Remobilization of andesite magma by intrusion of mafic magma at the Soufriere Hills volcano, Montserrat, West Indies. *Journal of Petrology*, 41, 21–42.
- Neave, D.A., and Putirka, K.D. (2017) A new clinopyroxene-liquid barometer, and implications for magma storage pressures under Icelandic rift zones. *American Mineralogist*, 102, 777–794.
- Putirka, K. (2016) Amphibole thermometers and barometers for igneous systems and some implications for eruption mechanisms of felsic magmas at arc volcanoes. *American Mineralogist*, 101, 841–858.
- Putirka, K.D., Canchola, J., Rash, J., Smith, O., Torrez, G., Paterson, S.R., and Ducea, M.N. (2014) Pluton assembly and the genesis of granitic magmas: Insights from the GIC pluton in cross section, Sierra Nevada Batholith, California. *American Mineralogist*, 99, 1284–1303.
- Ridolfi, F., and Renzulli, A. (2012) Calcic amphiboles in calc-alkaline and alkaline magmas: thermobarometric and chemometric empirical equations valid up to 1130 °C and 2.2 GPa. *Contributions to Mineralogy and Petrology*, 163, 877–895.
- Ridolfi, F., Renzulli, A., and Puerini, M. (2010) Stability and chemical equilibrium of amphibole in calc-alkaline magmas: an overview, new thermobarometric formulations and application to subduction-related volcanoes. *Contributions to Mineralogy and Petrology*, 160, 45–66.
- Sambridge, M.S., and Compston, W. (1994) Mixture modeling of multi-component datasets with application to ion probe zircon ages. *Earth and Planetary Science Letters*, 128, 373–390.
- Shimizu, K., Liang, Y., Sun, C., Jackson, C.R., and Saal, A.E. (2017) Parameterized lattice strain models for REE partitioning between amphibole and silicate melt. *American Mineralogist*, 102, 2254–2267.
- Sláma, J., Košler, J., Condon, D.J., Crowley, J.L., Gerdes, A., Hanchar, J.M., Horstwood, M.S.A., Morris, G.A., Nasdala, L., Norberg, N., Schaltegger, U., Schoene, B., Tubrett, M.N., and Whitehouse, M.J. (2008) Plešovice zircon— a new natural reference material for U-Pb and Hf isotopic microanalysis. *Chemical Geology*, 249, 1–35.
- Snyder, D. (2000) Thermal effects of the intrusion of basaltic magma into a more silicic magma chamber and implications for eruption triggering. *Earth and Planetary Science Letters*, 175, 257–273.
- Sparks, R.S.J., and Cashman, K.V. (2017) Dynamic magma systems: implications for forecasting volcanic activity. *Elements*, 13, 35–40.
- Sparks, R.S.J., Annen, C., Blundy, J.D., Cashman, K.V., Rust, A.C., and Jackson, M.D. (2019) Formation and dynamics of magma reservoirs. *Philosophical Transactions of The Royal Society A*, 377, 20180019.
- Sun, S.-S., and McDonough, W.F. (1989) Chemical and isotopic systematics of oceanic basalts: implications for mantle composition and processes. *Geological Society, London, Special Publications*, 42, 313–345.
- Till, C.B., Vazquez, J.A., Stelten, M.E., Shamloo, H.I., and Shaffer, J.S. (2019) Coexisting discrete bodies of rhyolite and punctuated volcanism characterize Yellowstone's post-Lava Creek Tuff caldera evolution. *Geochemistry, Geophysics, Geosystems*, 20.
- Van Orman, J.A., Cerniak, D.J., and Kita, N.T. (2014) Magnesium diffusion in plagioclase: dependence on composition, and implications for thermal resetting of the <sup>26</sup>Al-<sup>26</sup>Mg early solar system chronometer. *Earth and Planetary Science Letters*, 385, 79–88.



- Wang, R., Richards, J.P., Zhou, L.M., Hou, Z.Q., Stern, R.A., Creaser, R.A., and Zhu, J.J. (2015) The role of Indian and Tibetan lithosphere in spatial distribution of Cenozoic magmatism and porphyry Cu-Mo deposits in the Gangdese belt, southern Tibet. *Earth Science Reviews*, 150, 68–94.
- Wark, D.A., and Watson, E.B. (2006) TitaniQ: a titanium-in-quartz geothermometer. *Contributions to Mineralogy and Petrology*, 152, 743–754.
- Wark, D.A., Hildreth, W., Spear, F.S., Cherniak, D.J., and Watson, E.B. (2007) Pre-eruption recharge of the Bishop magma system. *Geology*, 35, 235–238.
- Waters, L.E., and Lange, R.A. (2015) An updated calibration of the plagioclase-liquid hygrometer-thermometer applicable to basalts through rhyolites. *American Mineralogist*, 100, 2172–2184.
- Weis, D., Kieffer, B., Maerschalk, C., Pretorius, W., and Barling, J. (2005) High-precision Pb-Sr-Nd-Hf isotopic characterization of USGS BHVO-1 and BHVO-2 reference materials. *Geochemistry, Geophysics, Geosystems*, 6, Q02002.
- Wendt, I., and Carl, C. (1991) The statistical distribution of the mean squared weighted deviation. *Chemical Geology: Isotope Geoscience Section*, 86, 275–285.
- Werts, K., Barnes, C.G., Memeti, V., Ratschbacher, B., Williams, D., and Paterson, S.R. (2020) Hornblende as a tool for assessing mineral-melt equilibrium and recognition of crystal accumulation. *American Mineralogist*, 105, 77–91.
- Wood, B.J., and Blundy, J.D. (1997) A predictive model for rare earth element partitioning between clinopyroxene and anhydrous silicate melt. *Contributions to Mineralogy and Petrology*, 129, 166–181.
- Wu, F.Y., Liu, X.C., Ji, W.Q., Wang, J.M., and Yang, L. (2017) Highly fractionated granites: recognition and research. *Science China Earth Sciences*, 60, 1201–1219.
- Zhang, X.Q., Zhu, D.C., Zhao, Z.D., Sui, Q.L., Wang, Q., Yuan, S.H., Hu, Z.C., and Mo, X.X. (2012) Geochemistry, zircon U-Pb geochronology and in-situ Hf isotope of the Maiga batholith in Coqen, Tibet: constraints on the petrogenesis of the Early Cretaceous granitoids in the central Lhasa Terrane. *Acta Petrologica Sinica*, 28, 1615–1634 (in Chinese with English abstract).
- Zhang, J., Humphreys, M.C.S., Cooper, G.F., Davidson, J.P., and Macpherson, C.G. (2017) Magma mush chemistry at subduction zones, revealed by new melt major element inversion from calcic amphiboles. *American Mineralogist*, 102, 1353–1367.
- Zhang, L., Ren, Z.Y., Xia, X.P., Yang, Q., Hong, L.B., and Wu, D. (2019) In situ determination of trace elements in melt inclusions using laser ablation inductively coupled plasma sector field mass spectrometry. *Rapid Communications in Mass Spectrometry*, 33, 361–370.
- Zhou, J.-S., Wang, Q., Wyman, D.A., and Zhao, Z.-H. (2020a) Petrologic reconstruction of the Tieshan magma plumbing system: Implications for the genesis of magmatic-hydrothermal ore deposits within originally water-poor magmatic systems. *Journal of Petrology*, <https://doi.org/10.1093/ptrology/egaa056>
- Zhou, J.-S., Yang Z.-S., Hou, Z.-Q., and Wang, Q. (2020b) Amphibole-rich cumulate xenoliths in the Zhazhalong intrusive suite, Gangdese arc: Implications for the role of amphibole fractionation during magma evolution. *American Mineralogist*, 105, 262–275.
- Zhu, D.C., Zhao, Z.D., Niu, Y., Mo, X.X., Chung, S.L., Hou, Z.Q., Wang, L.Q., and Wu, F.Y. (2011) The Lhasa Terrane: record of a microcontinent and its histories of drift and growth. *Earth and Planetary Science Letters*, 301, 241–255.
- Zhu, D.C., Wang, Q., Zhao, Z.D., Chung, S.L., Cawood, P.A., Niu, Y., Liu, S.A., Wu, F.Y., and Mo, X.X. (2015) Magmatic record of India-Asia collision. *Scientific Reports*, 5, 14289.
- Zhu, D.C., Wang, Q., Cawood, P.A., Zhao, Z.D., and Mo, X.X. (2017) Raising the Gangdese Mountains in southern Tibet. *Journal of Geophysical Research: Solid Earth*, 122, 214–223.

MANUSCRIPT RECEIVED NOVEMBER 16, 2019

MANUSCRIPT ACCEPTED MARCH 18, 2020

MANUSCRIPT HANDLED BY CALVIN BARNES

### Endnote:

<sup>1</sup>Deposit item AM-20-107369, Supplemental Material. Deposit items are free to all readers and found on the MSA website, via the specific issue's Table of Contents (go to [http://www.minsocam.org/MSA/AmMin/TOC/2020/Oct2020\\_data/Oct2020\\_data.html](http://www.minsocam.org/MSA/AmMin/TOC/2020/Oct2020_data/Oct2020_data.html)).